RSC Advances

PAPER

View Article Online
View Journal | View Issue

Cite this: *RSC Adv.*, 2026, **16**, 29611

One-pot fabrication of a novel urchin-like Fe_3O_4/α-FeOOH/$Al(OH)_3$ magnetic nanocomposite for phosphate removal and recovery: adsorption performance and mechanism

Yu-Han Wang,[ab] Wei Yin,[ab] Wen-Ping Liu,[ab] Qi-Zhi Yao,[c] Sheng-Quan Fu[d] and Gen-Tao Zhou *[ab]

Driven by the dual crises of global phosphorus depletion and severe aquatic eutrophication, developing sustainable technologies for phosphorus recovery is of paramount importance. Herein, we report a facile one-pot synthesis of a novel magnetic adsorbent Fe_3O_4/α-FeOOH/$Al(OH)_3$ (MGA) nanocomposite, wherein amorphous aluminum hydroxide is uniformly coated onto an urchin-like magnetite/goethite carrier. Systematic optimization of the $Al(OH)_3$ loading demonstrated that the optimal composite delivered a maximum phosphate adsorption capacity of 94.9 mg-P g^{-1} with a partition coefficient of 0.53 mg g^{-1} μM^{-1} at pH 7.0. MGA exhibited favorable adsorption performance across a pH range from 6.0 to 10.0, and was virtually unaffected by ubiquitous competing anions (Cl^-, NO_3^-, SO_4^{2-}, HCO_3^-, and CH_3COO^-). Comparative spectroscopic investigations (XPS and FTIR) of the pristine and spent materials elucidated that this exceptional affinity primarily stems from a combination of electrostatic attractions and ligand exchange, leading to the formation of inner-sphere complexes. Desorption tests revealed that MGA sustained a competitive adsorption capacity over five regeneration cycles. Overall, MGA represents an economically viable and highly efficient candidate for the remediation of phosphorus-polluted waters and subsequent resource recovery.

Received 5th March 2026
Accepted 24th May 2026

DOI: 10.1039/d6ra01891b

rsc.li/rsc-advances

1. Introduction

Phosphorus (P), an essential nutrient for biosynthesis and energy transfer in living organisms, is extensively mined from geological deposits to produce agricultural fertilizers that meet global food demands.[1] Such industrial and agricultural activities accelerate the unidirectional flow of phosphorus from the lithosphere to the biosphere and hydrosphere, disrupting the natural phosphorus cycle and driving the rapid depletion of this non-renewable resource, with a risk of exhaustion within decades.[1–4] Furthermore, excessive phosphorus entering aquatic environments often induces eutrophication, resulting in harmful algal blooms and degraded water quality.[5,6] Particularly in chronically eutrophic water bodies, the release of legacy phosphorus from sediments (*i.e.*, internal phosphorus loading) severely hinders the rapid recovery of water quality, even when external phosphorus inputs are effectively controlled.[7] This dual crisis of phosphorus resource depletion and eutrophication underscores the urgent need for sustainable technologies to remove and recover phosphorus from polluted waters.

Adsorption is widely recognized as a viable technique for phosphorus removal and recovery, offering distinct advantages such as high selectivity, low cost, and operational simplicity.[8–10] Among various adsorbents, magnetic materials stand out due to their ease of separation and rapid recovery under an external magnetic field, demonstrating considerable potential in phosphorus recovery applications.[11–14] Recently, lanthanum (La)-based magnetic adsorbents have garnered significant attention owing to the strong chemical affinity of lanthanum for phosphate.[15–20] However, excessive reliance on La-bearing materials introduces substantial challenges: the unsustainable consumption of rare earth resources and high material costs critically undermine their economic viability.[15,21,22] In response, recent studies have explored the incorporation of low-cost aluminum (Al) into La-based materials to develop La-Al composite adsorbents, aiming to reduce costs while preserving high adsorption performance.[22–24] Beyond the economic considerations, another practical challenge associated with La-based materials lies in their limited reversibility.

[a]*Deep Space Exploration Laboratory/School of Earth and Space Sciences, University of Science and Technology of China, Hefei 230026, China. E-mail: gtzhou@ustc.edu.cn; Fax: +86 551 63600533; Tel: +86 551 63600533*

[b]*State Key Laboratory of Lithospheric and Environmental Coevolution, University of Science and Technology of China, Hefei 230026, China*

[c]*School of Chemistry and Materials Science, University of Science and Technology of China, Hefei 230026, China*

[d]*Hefei National Laboratory for Physical Sciences at the Microscale, University of Science and Technology of China, Hefei 230026, China*

While they effectively immobilize phosphate, the formation of quasi-insoluble $LaPO_4 \cdot nH_2O$ necessitates very acidic or basic pH conditions (*i.e.*, pH < 2 or pH > 13) for phosphate desorption, thereby hindering sustainable phosphorus recycling.[25,26]

Rather than treating aluminum merely as a low-cost additive, revisiting its well-established application in lake restoration provides an alternative perspective. For decades, aluminum salts have been widely dosed into eutrophic lakes globally to immobilize phosphate *via* the abundant binding sites of *in situ* formed amorphous $Al(OH)_3$.[27–30] However, due to the amphoteric nature of aluminum hydroxides, it is highly susceptible to redissolution triggered by pH fluctuations, posing a risk of secondary release of the *in situ* immobilized phosphorus from the immobilized sediment.[31] In this context, integrating amorphous $Al(OH)_3$ with magnetic substrates enables prompt magnetic separation of spent $Al(OH)_3$, thereby not only mitigating this environmental risk but also facilitating efficient phosphorus recovery upon separation.

However, the direct combination of $Al(OH)_3$ and Fe_3O_4 nanoparticles often results in severe aggregate due to their high surface energy,[24] which masks the active sites and drastically reduces the effective adsorption capacity of the composite.[19,24] To address this limitation, a surface-coating strategy, wherein $Al(OH)_3$ is uniformly deposited onto an appropriate supporting substrate, can not only increase the available loading but also effectively suppress nanoparticle aggregation, thereby significantly enhancing the adsorption performance.[32,33] Among various candidate carriers, goethite (α-FeOOH), one of the most common and thermodynamically stable iron oxide minerals in nature, presents distinct advantages.[34,35] Structurally, the close similarities in chemical properties and ionic radii between Al^{3+} and Fe^{3+} facilitate the isomorphous substitution of Al^{3+} into goethite lattice and the attachment of Al^{3+} onto the surface of goethite.[36–38] Moreover, goethite and magnetite share highly compatible synthesis pathways. By controlling the oxidation conditions of the initial precipitates formed upon mixing alkaline and Fe(II) solutions, these two iron oxides can be easily co-synthesized.[39–42] This not only provides a promising and straightforward route for constructing an ideal "magnetite/goethite" composite support, while also minimizing the risk of secondary environmental pollution associated with the introducing of foreign elements. In view of these advantages, this study aims to: (1) develop a facile one-pot strategy to fabricate a novel magnetic adsorbent by coating $Al(OH)_3$ onto an urchin-like Fe_3O_4/α-FeOOH composite support (denoted as MGA, *i.e.*, Fe_3O_4/α-FeOOH/$Al(OH)_3$); (2) systematically evaluate its phosphorus adsorption and recovery performance in aqueous solutions; and (3) elucidate the underlying adsorption mechanism through the structural characterization and functional group analysis of both pristine and spent MGA materials.

2. Experimental section

2.1 Chemicals and materials

All reagents ($FeSO_4 \cdot 7H_2O$, $Al_2(SO_4)_3 \cdot 18H_2O$, CH_3COONa, and KH_2PO_4) were of analytical purity, obtained from Sinopharm Chemical Reagent Co., Ltd, and applied without subsequent purification. A standard stock solution containing 1000 mg-P L^{-1} was generated by dissolving 1.1090 g KH_2PO_4 in 250 mL deionized water.

2.2 Synthesis of adsorbents

The Fe_3O_4/α-FeOOH/$Al(OH)_3$ nanocomposite was synthesized *via* a facile one-pot method. In a typical procedure, 1.39 g of $FeSO_4 \cdot 7H_2O$ and 0.82 g of CH_3COONa were dissolved in 50 mL of deionized water. This solution was transferred into a 100 mL, three-necked, round-bottomed flask equipped with a vertical mechanical agitator and subsequently heated in a water bath at 60 °C under continuous stirring (200 rpm). After 1 h of stirring, two separate 10 mL aqueous solutions containing 0.67 g of $Al_2(SO_4)_3 \cdot 18H_2O$ and 0.49 g of CH_3COONa were sequentially added dropwise into the mixture. The resulting suspension was allowed to react under continuous stirring for an additional 1 h. The obtained precipitate was collected *via* magnetic separation, washed thoroughly with deionized water and absolute ethanol several times, and finally dried overnight in a vacuum oven at 40 °C. By varying the added amounts of $Al_2(SO_4)_3 \cdot 18H_2O$ and CH_3COONa, a series of composites with Al-to-Fe molar percentages of 10, 20, 30, 40, and 50 mol% were synthesized. These samples were designated as MGA10, MGA20, MGA30, MGA40, and MGA50, respectively. The actual $Al(OH)_3$ content in the synthesized MGA adsorbents was determined using inductively coupled plasma mass spectrometry (ICP-MS), with the results summarized in Table S1 of the SI.

To synthesize the bare magnetite/goethite nanocomposite (denoted as MG), a mixed solution of $FeSO_4 \cdot 7H_2O$ and CH_3COONa was continuously stirred for 2 h at 60 °C with a stirring speed of 200 rpm. Subsequently, the resulting precipitate was collected, washed, and dried following the same protocol described above. The detailed optimization processes, including the oxidation of Fe(II) under various temperatures and stirring speeds and the characterization of those oxidation products, are provided in the SI (Text S1 and Fig. S1).

2.3 Characterizations

The crystalline composition and structure of the precipitated samples were characterized by powder X-ray diffraction (XRD, Rigaku Smart Lab, Japan) operated at 40 kV and 200 mA, Cu Kα irradiation, $\lambda = 0.154056$ nm. Morphological observations and microstructural details were acquired *via* cold field-emission scanning electron microscopy (FESEM, HITACHI SU8220, Japan) and transmission electron microscopy (TEM, JEM-2100Plus, Japan) at accelerating voltages of 2.0 and 200 kV, respectively. Concurrently, elemental mapping was performed using an X-MAX energy-dispersive X-ray spectroscopy (EDS) detector integrated into the FESEM system (operated at 15.0 kV). Surface functional groups and chemical states of the constituent elements were identified by Fourier transform infrared (FT-IR, Nicolet iS10) and X-ray photoelectron spectroscopy (XPS, ESCALAB 250), both supplied by Thermo Scientific, USA. The magnetic separation capability was evaluated at 300 K with a vibrating sample magnetometer (VSM, MPMS3, Quantum Design, USA). The zeta potential of the MGA

adsorbents was measured using a Brookhaven NanoBrook Omni zeta potential analyzer.

2.4 Batch adsorption experiments

Batch experiments were conducted to evaluate the phosphate adsorption performance of the MGA nanocomposite. In a typical procedure, 0.010 g of adsorbent was dispersed into 100 mL of phosphate solution with various concentrations and pH values in glass bottles. The initial pH was adjusted using diluted HCl or NaOH solution. The mixture was continuously agitated at 200 rpm in a thermostatic shaker maintained at 25 °C. Based on the results of kinetics, a contact time of 24 h was employed to ensure adsorption equilibrium before the suspension was filtered through a 0.22 μm mixed cellulose ester membrane. The residual phosphate concentration in the filtrates was quantified at 880 nm *via* the molybdenum blue spectrophotometric method[43] using a TU-1901 UV-vis spectrophotometer. All the batch experiments were carried out in triplicate, and the results were presented as mean values with standard deviations.

Kinetic experiments were performed at pH 7.0 with an initial phosphate concentration of 10 mg-P L^{-1}. At designated time intervals (1, 5, 10, 30, 60, 180, 360, 720, 1440, and 2880 min), 2 mL aliquots of the suspension were extracted for analysis. The time-dependent adsorption data were subsequently modeled using the pseudo-first-order (eqn (1)) and pseudo-second-order (eqn (2)) equations:

$$\frac{dQ_e}{dt} = k_1\ (Q_e - Q_t) \tag{1}$$

$$\frac{dQ_e}{dt} = k_2\ (Q_e - Q_t)^2 \tag{2}$$

where k_1 (min^{-1}) and k_2 (g mg^{-1} min^{-1}) denote the respective rate constants; Q_e (mg g^{-1}) and Q_t (mg g^{-1}) represent the quantities of phosphate adsorbed by the MGA composite at equilibrium and at time t (min), respectively.

Adsorption isotherms were obtained by varying the initial phosphate concentrations from 0 to 15 mg-P L^{-1} at pH 7.0, with an equilibration time of 24 h. The experimental data were subsequently fitted to the Langmuir (eqn (3)) and Freundlich (eqn (4)) models:

$$Q_e = \frac{Q_{max} K_L C_e}{1 + K_L C_e} \tag{3}$$

$$Q_e = K_F C_e^{\,n} \tag{4}$$

where Q_e (mg-P g^{-1}) and C_e (mg L^{-1}) represent the equilibrium adsorption capacity and the residual phosphate concentration in the solution, respectively; K_L (L mg^{-1}) is the Langmuir constant, and Q_{max} (mg-P g^{-1}) denotes the maximum phosphate sorption capacity; K_F (mg^{1-n} L^n g^{-1}) is the Freundlich constant related to the adsorption capacity, and n indicates the adsorption intensity.

The time-dependent adsorption capacity Q_t (mg g^{-1}), equilibrium adsorption capacity Q_e (mg g^{-1}), and partition coefficient PC (mg g^{-1} μM^{-1}) were determined using the following equations:

$$Q_t = \frac{(C_0 - C_t)V}{m} \tag{5}$$

$$Q_e = \frac{(C_0 - C_e)V}{m} \tag{6}$$

$$PC = \frac{Q_e}{C_e} \times \frac{31}{1000} \tag{7}$$

where C_0, C_t, and C_e (mg-P g^{-1}) denote the aqueous phosphate concentrations initially, at a given time t(min), and at equilibrium, respectively; V (L) and m (g) represent the volume of the working solution and the dry mass of the added adsorbent, respectively; the coefficient 31 in eqn (7) corresponds to the atomic weight of phosphorus, applied here for molar unit conversion.

The effect of initial pH on adsorption was investigated with a phosphate concentration of 10 mg-P L^{-1} in a pH range of 4–11. To investigate the selectivity of MGA for phosphate adsorption, competitive adsorption experiments were conducted through the addition of common coexisting anions, such as Cl^-, NO_3^-, SO_4^{2-}, HCO_3^- or CH_3COO^-, into the phosphate solutions at different concentrations (10 and 100 mg L^{-1}).

For desorption assays, MGA40 was pre-loaded with phosphate (10 mg-P L^{-1}). The spent adsorbent was then magnetically separated, washed thrice with deionized water, and resuspended in NaOH solutions for phosphate release. The desorption efficiency R_d (%) was determined by quantifying the desorbed phosphate in the supernatant, calculated as:

$$R_d\ (\%) = \frac{C_d \times V_d}{(C_0 - C_e) \times V} \times 100 \tag{8}$$

where C_d (mg L^{-1}) represents the phosphate concentration in the desorption solution. V_d and V (L) denote the volumes of the desorption and initial adsorption solutions, respectively; C_0, and C_e (mg-P L^{-1}) are the phosphate concentrations at the initial time and equilibrium, respectively. After determining suitable desorption conditions, five adsorption–desorption cycles were conducted.

3. Results and discussion

3.1 Characterization of the MG and MGA40 nanocomposite

Demonstrating an optimal balance between material loading and phosphate adsorption performance, MGA40 achieved near-maximum capacity without redundant aluminum addition (Fig. S2) and was thus selected as the representative sample for characterization alongside pristine MG without Al loading. As illustrated in Fig. 1, the X-ray diffraction (XRD) pattern of MG displays characteristic peaks that can be indexed to a mixed phase of magnetite (Fe_3O_4, cubic crystal system with space group Fd-3m, JCPDS No. 19-0629) and goethite (α-FeOOH, orthorhombic crystal system with space group Pbnm, JCPDS No. 29-0713). Notably, while the MGA40 composite preserves the same phase composition, it lacks characteristic diffraction peaks corresponding to crystalline aluminum-containing

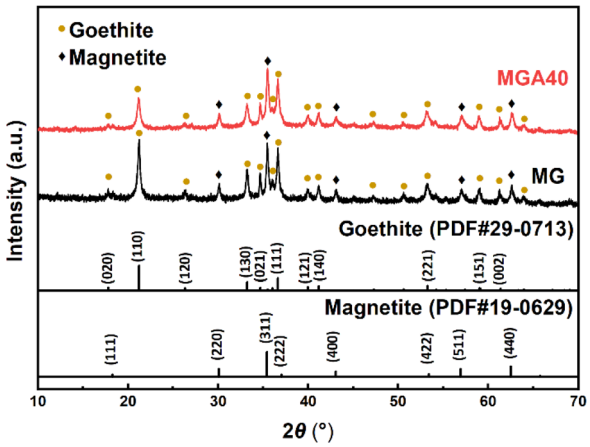

Fig. 1 XRD patterns of MG and MGA40 nanocomposites.

phases. This absence strongly implies that the aluminum species predominantly exist in an amorphous state within the nanocomposite. To verify this, a sample without the MG substrate was synthesized under the identical conditions. Its XRD pattern (Fig. S3) exhibits only a broad amorphous halo devoid of sharp peaks, confirming that the formed aluminum species are intrinsically amorphous.

The morphological features and surface textures of MG and MGA40 were observed using FESEM and TEM. Low magnification SEM observations exhibit that the MG nanocomposite is composed of urchin-like hierarchical architectures with a diameter of approximately 1 μm (*e.g.*, Fig. 2a). The locally magnified results further reveal that these urchin-like structures are radially assembled from needle-like nanorods with ~500 nm in length and ~50 nm in diameter (*e.g.*, Inset in Fig. 2a). TEM analysis (Fig. 2b) not only corroborates the interlacing nature of these nanorods but also reveals some nanoparticles (~40 nm in diameter) that were unresolved by FESEM. These nanoparticles are predominantly localized at the central intersecting cores of the nanorod assemblies, with a minor fraction scattered along the outer periphery. For the aluminum-modified sample, the FESEM image of MGA40 (Fig. 2c) exhibits a distinct morphological transition. Specifically, compared to the smooth surfaces and sharp edges of the pristine MG nanorods, the modified nanorods display noticeably roughened surfaces and blunted edges. Corresponding EDS elemental mapping (Fig. 2d) demonstrates that the Al signal spatially overlaps with the Fe and O distributions and strictly follows the structural contour of the entire urchin-like architectures without any localized independent aggregations, indicating a homogeneous distribution of aluminum species on MG substrate. TEM analyses of MGA40 (Fig. 2e) further validate this surface roughening. Compared with the MG nanocomposite (Fig. 2b), a disordered amorphous overlayer can be clearly observed enveloping the rods (Fig. 2e), perfectly aligning with the texture captured by FESEM. Combining with the EDS elemental mapping (Fig. 2d), it can be concluded that the amorphous overlayers should be aluminum (oxy)hydroxides. High-resolution TEM (HRTEM, Fig. 2f) resolves distinct lattice fringes with interplanar spacings of 0.296 nm in the core nanoparticles and 0.219 nm in the nanorods, which correspond to the (220) plane of magnetite and the (140) plane of goethite, confirming that the particles and rods are magnetite and goethite, respectively, consistent with their intrinsic growth habits. Together, the morphological and elemental analyses demonstrate that the amorphous aluminum phase is uniformly coated onto the MG support.

Fourier transform infrared (FT-IR) spectroscopy was employed to identify the functional groups and confirm the composition of the supported aluminum phase (Fig. 3a). In the spectra of both MG and MGA40, the characteristic absorption bands at 891 and 790 cm^{-1} are assigned to the O–H bending vibrations of α-FeOOH,[44,45] while the band at 574 cm^{-1} corresponds to the Fe–O stretching vibration of Fe_3O_4.[45] These observations are highly consistent with the XRD and HRTEM results. For the MGA40 composite, the emergence of a new absorption peak at 977 cm^{-1} is attributed to Al–O stretching, confirming the amorphous aluminum hydroxide ($Al(OH)_3$) formation.[46,47] Furthermore, the band at 1090 cm^{-1}, associated with the symmetrical vibration of surface Al–OH groups, further confirms the presence of $Al(OH)_3$.[48–50] Additionally, the C–H stretching vibrations at 2919 and 2850 cm^{-1},[51] along with the distinctive bands at 1577 and 1466 cm^{-1} assigned to Al-coordinated acetate complexes,[50,52,53] suggest that residual acetate from the precursor remains on the $Al(OH)_3$ surface, likely forming bridging complexes with Al.

Furthermore, in comparison with the XPS survey of the MG nanocomposites, an additional Al peak was detected alongside Fe and O in the MGA40 nanocomposite (Fig. S4). The high-resolution Al 2p XPS spectrum shows that the binding energy is 75.05 eV (Fig. 3b), higher than the reported Al 2p peak at 74.1 eV from amorphous $Al(OH)_3$.[50] To identify the specific chemical states, the spectrum was deconvoluted into two subpeaks located at 74.5 eV and 75.3 eV. The component at 74.5 eV is attributed to the Al–O bonds in aluminum hydroxides.[54–56] The higher binding energy peak at 75.3 eV is ascribed to the Al–O–C bonds.[57] The assignment of this high-energy component is consistent with the FTIR results, further confirming the strong interfacial interaction between the surface acetate groups and Al species. Overall, the consistent results from both XPS and FT-IR characterizations demonstrate that the aluminum phase on the MGA40 surface is indeed amorphous $Al(OH)_3$, enriched with active surface hydroxyl groups and coordinated acetate ligands.

To further understand the pore structures of the synthesized materials, nitrogen adsorption–desorption analysis was performed. As depicted in Fig. 4a, the isotherms of both the MG and the MGA40 composite exhibit classical type IV curves with distinct H3-type hysteresis loops at high relative pressures over 0.6. According to the IUPAC classification, this indicates the presence of abundant mesopores, possibly originating from the slit-shaped pores containing mesopores formed by the aggregated goethite nanorods.[58] After the coating process, the BET specific surface area of MGA40 remarkably increases to 77.98 $m^2 g^{-1}$, almost doubling the value of 37.79 $m^2 g^{-1}$ measured for the MG support (Table S2). The corresponding pore size

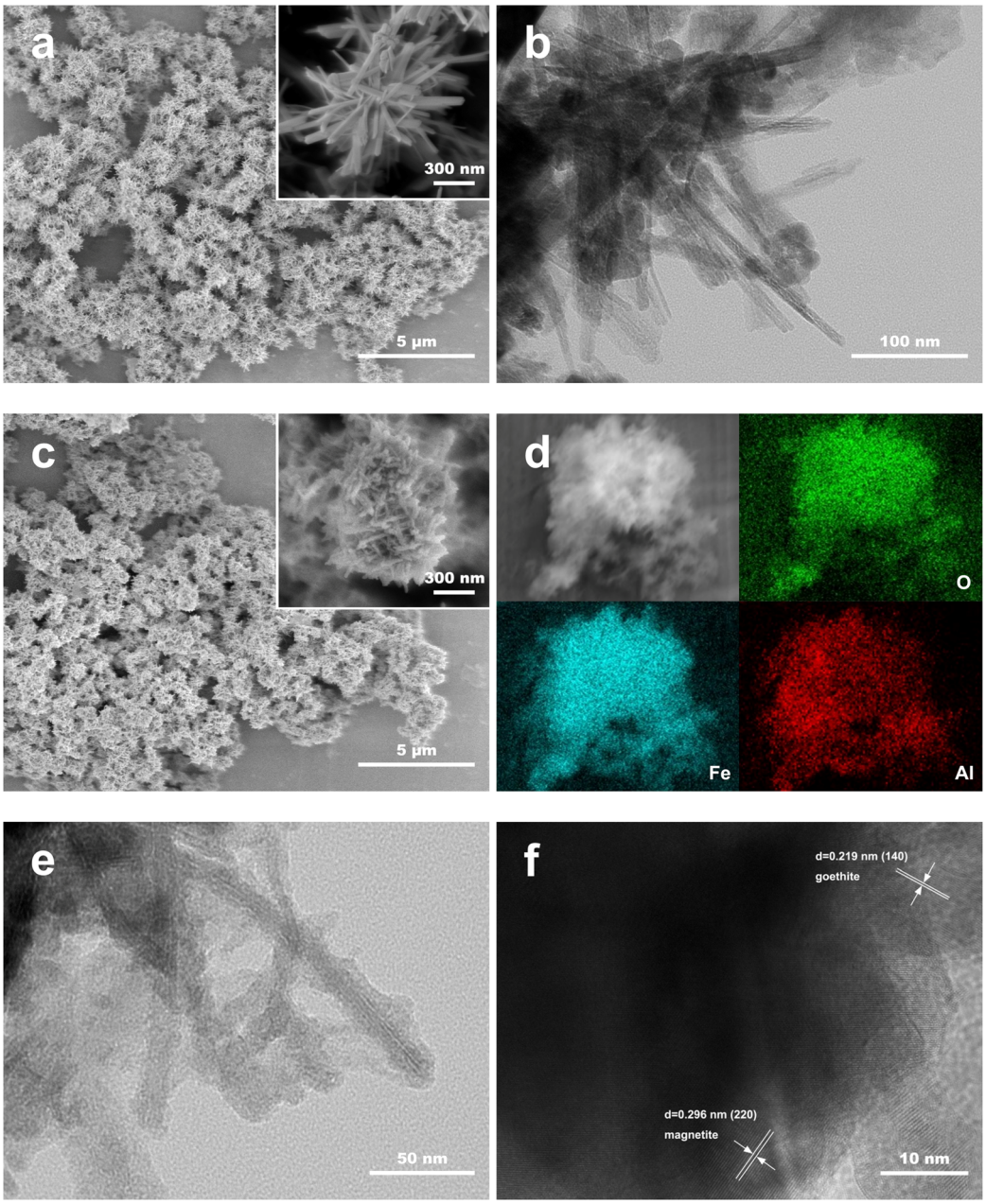

Fig. 2 FESEM (a) and TEM (b) images of MG nanocomposites. FESEM image (c), O, Fe, and Al elemental mappings (d), TEM (e) and HRTEM (f) images of MGA40 nanocomposite.

distribution curves (Inset in Fig. 4a) further confirm this structural modification. While the MG displays a broad distribution of large mesopores ranging from 20 to 50 nm, MGA40 exhibits a remarkably sharp and intense peak in the micro- and small-mesopore region below 5 nm. This indicates that the introduction of amorphous coating accounts for the nearly doubled specific surface area.

Moreover, magnetic properties of MG and MGA40 samples were evaluated at room temperature under an applied magnetic field of up to ±30 000 Oe. As depicted in Fig. 4b, the MG carrier exhibits a saturation magnetization (M_s) of 35.8 emu per g, with a remanent magnetization (M_r) of 6.19 emu per g and coercivity (H_c) of 97.2 Oe, while the MGA40 nanocomposite shows an M_s of 13.5 emu per g, M_r of 2.14 emu per g, and H_c of 84.9 Oe. Both samples exhibit narrow hysteresis loops with relatively low coercivity and remanent magnetization, indicating soft magnetic behavior. The M_s of the bare MG carrier is lower than that of pure Fe_3O_4 nanoparticles reported in the literature.[20,59] This reduction is primarily attributed to the mass dilution effect caused by the co-synthesized α-FeOOH phase. Following the loading of amorphous $Al(OH)_3$, the M_s of the MGA40 nanocomposite further decreased to approximately 13.5 emu per g due to the additional mass contribution from this non-magnetic component. Nevertheless, this M_s value remains

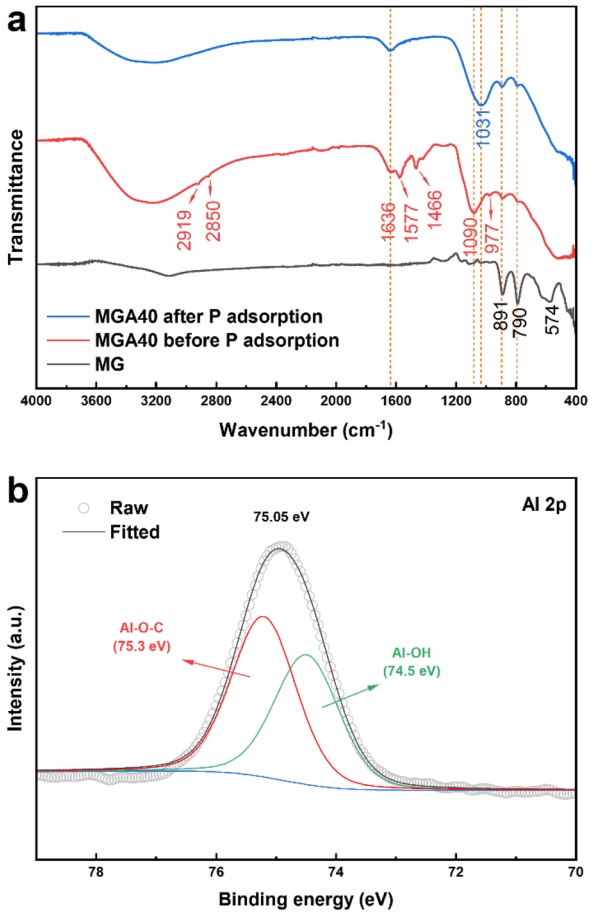

Fig. 3 FT-IR spectra (a) of MG and MGA40 nanocomposites before and after phosphate adsorption, and deconvoluted high-resolution Al 2p XPS spectrum (b) of MGA40 nanocomposite.

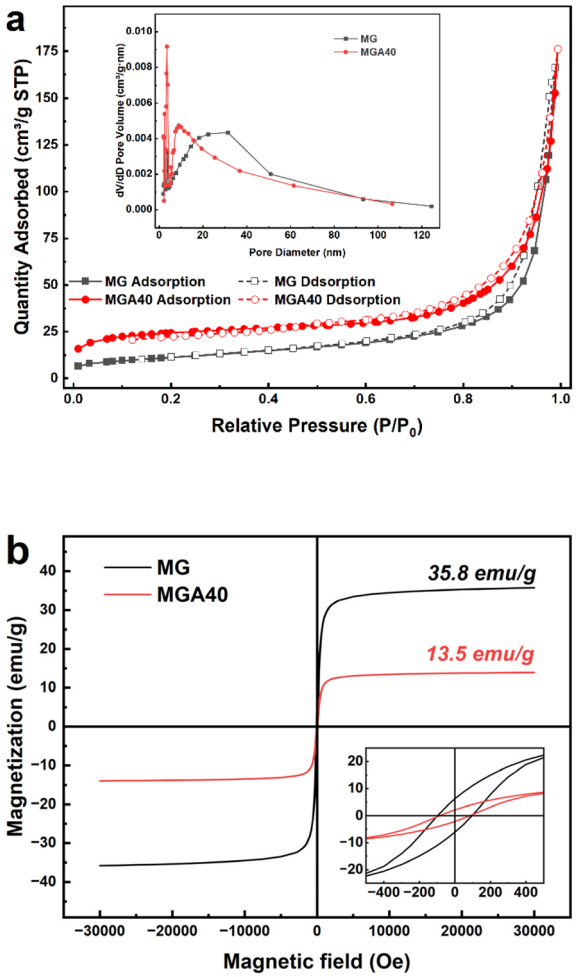

Fig. 4 N_2 adsorption–desorption isotherm with pore size distribution (a) and magnetic hysteresis loops (b) of MG and MGA40 nanocomposites.

entirely sufficient for rapid solid–liquid separation. Comparable or even lower M_s values have been reported for magnetically recoverable composite adsorbents, such as 13.3 emu per g for $La(OH)_3/Fe_3O_4$ (4 : 1) and 11.25 emu per g for $NaCe(CO_3)_2/Fe_3O_4$, further supporting the adequacy of the magnetic responsiveness observed in this study.[20,59]

3.2 Effect of aluminum loading of MGA on phosphorus adsorption

To elucidate the adsorption kinetics of phosphate onto MGA nanocomposites with varying compositions, time-dependent adsorption experiments were conducted. As depicted in Fig. 5a, phosphate adsorption by all investigated nanocomposites exhibited an initial rapid adsorption phase, ultimately plateauing and reaching adsorption equilibrium at approximately 24 h. For further insight into the kinetic mechanism, the experimental data were fitted using pseudo-first-order and pseudo-second-order models. As detailed in Table 1 and S3, the correlation coefficients (R^2) for the pseudo-second-order model (0.9435–0.9603) were consistently higher than those for the pseudo-first-order model (0.9140–0.9297). Moreover, the theoretical equilibrium adsorption capacities calculated from the pseudo-second-order model (38.99–81.44 mg g^{-1}) were closer to the experimental data (40.13–84.22 mg g^{-1}) than those from the pseudo-first-order model (37.12–77.89 mg g^{-1}). Collectively, these results indicate that the adsorption process follows pseudo-second-order kinetics and is primarily governed by chemisorption, involving the formation of chemical bonds between phosphate ions and active surface sites.[60] Notably, as the $Al(OH)_3$ content increased from 10% to higher loadings, the predicted equilibrium adsorption capacity (Q_e) of MGA significantly increased from 38.99 to 81.44 mg-P g^{-1}, while the adsorption rate constant (k_2) exhibited a declining trend (Table 2). This inverse trend suggests that a higher $Al(OH)_3$ loading provides abundant active sites for phosphate adsorption and thus enhances the adsorption capacity. However, the resulting high surface coverage also intensifies both electrostatic repulsion and intraparticle diffusion resistance, thereby prolonging the time required to reach equilibrium and decreasing k_2.[61] Furthermore, different magnetic substrate materials may lead to distinct adsorption kinetic behaviors. Tan *et al.* developed nanoscale zero-valent iron-based NZVI@$Al(OH)_3$ magnetic materials for phosphate

Table 1 Fitted parameters for the pseudo-second-order kinetics and Freundlich isotherm of phosphate adsorption on MGA

	Pseudo-second-order kinetics			Freundlich isotherm		
Sorbents	k_2 [g (mg^{-1} min^{-1})]	Predicted q_e (mg-P g^{-1})	R^2	K_F (mg^{1-n} L^n g^{-1})	n	R^2
MGA10	1.15×10^{-3}	38.99	0.9435	31.137	0.136	0.9832
MGA20	8.05×10^{-4}	58.68	0.9498	50.688	0.120	0.9796
MGA30	7.17×10^{-4}	69.19	0.9414	64.917	0.131	0.9269
MGA40	6.82×10^{-4}	80.47	0.9654	76.758	0.146	0.9723
MGA50	6.58×10^{-4}	81.44	0.9603	78.038	0.148	0.9713

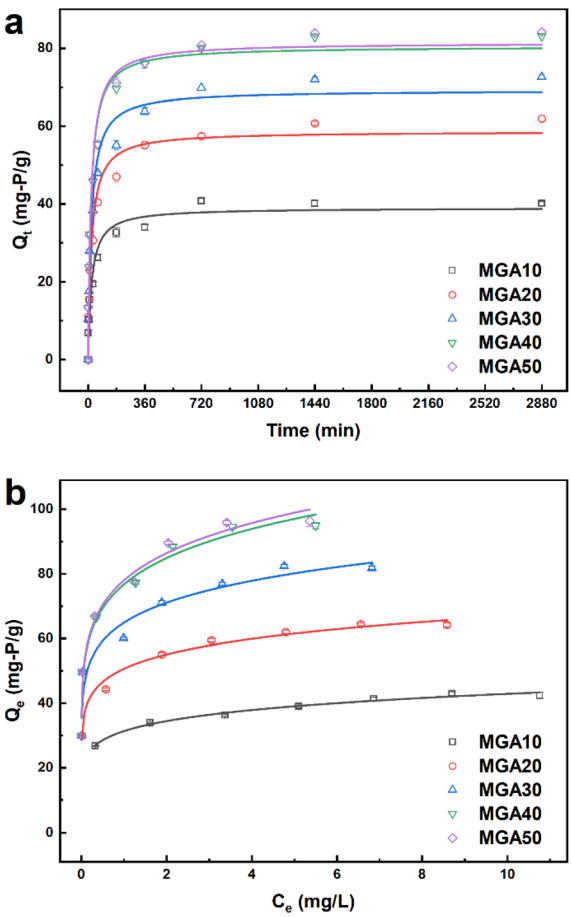

Fig. 5 Pseudo-second-order kinetics (a) and Freundlich isotherms (b) of phosphate adsorption by MGA nanocomposite.

adsorption; however, their kinetic performance was substantially affected by NZVI oxidation, leading to an initial decrease followed by an increase in both k_2 and Q_e with rising Al(OH)$_3$ content.[62] In contrast, the MGA nanocomposites employed in this study utilize magnetite and goethite, both inherently stable iron (oxy)hydroxides. The continuous improvement in kinetic performance observed for MGA is highly consistent with the enhanced phosphate adsorption reported for magnetite/La(OH)$_3$ hybrids as their active metal hydroxide content increases.[15,20] This alignment confirms that the enhanced phosphate sorption is mainly ascribed to the amorphous Al(OH)$_3$. Although goethite inherently possesses an affinity for phosphate *via* its surface hydroxyl groups, the adsorption capacity of bare goethite is relatively limited.[38,63,64] This limitation can be attributed to its well-crystallized structure, which typically offers a smaller specific surface area and fewer active sites compared to the disordered phases.[64] For instance, Hsu *et al.* reported a phosphate sorption capacity of only 135 mmol kg^{-1} (approximately 4.2 mg-P g^{-1}) for goethite,[38] and Zhang *et al.* demonstrated that well-crystallized α-FeOOH exhibits an equilibrium phosphate adsorption capacity of 13.65 mg g^{-1}, which is significantly lower than that of amorphous iron phases (98.69 mg g^{-1}).[63] Thus, well-crystallized goethite might contribute marginally to phosphate capture, acting primarily as a robust structural substrate in the MGA40 nanocomposite.

Phosphate adsorption isotherms were evaluated to determine the adsorption capacities of the MGA nanocomposites with varying Al(OH)$_3$ loadings. The results are depicted in Fig. 5b, with the corresponding fitted parameters summarized in Table 1 and S3. The Freundlich model outperformed the Langmuir model, yielding higher correlation coefficients (R^2) in the range of 0.9269–0.9832, compared to 0.6199–0.8883 for the latter. This superior fit indicates that phosphate adsorption onto the magnetic composites is a highly heterogeneous process and is not restricted to monolayer coverage.[65] As expected, the adsorption capacity increases with the Al(OH)$_3$ loading, reaching a maximum of 96.4 mg-P g^{-1} for MGA50 (Fig. 5b). This loading-dependent enhancement further confirms that phosphate adsorption is primarily governed by binding to the amorphous Al(OH)$_3$. However, MGA40 exhibits a highly comparable adsorption capacity of 94.9 mg-P g^{-1}. This plateau implies that the active sites on the MG carrier approach saturation at this loading ratio and further increasing the Al(OH)$_3$ content provides marginal enhancement in capacity. Consequently, MGA40 was identified as the optimal candidate for subsequent experiments.

While maximum capacity reflects the overall adsorption performance, it is highly dependent on specific operating conditions.[66] Therefore, the partition coefficient (PC) is introduced alongside adsorption capacity to provide a more objective comparison of different adsorbents for phosphate removal. In a solid–liquid system, the PC is defined as the ratio of the adsorbate concentration in the solid phase to that in the equilibrium liquid phase, thereby reflecting the true performance of the adsorbent.[67] Table 2 compares the adsorption performance of MGA40 with other reported magnetic adsorbents. In terms of the maximum adsorption capacity, MGA40 is comparable or

Table 2 Comparison of P adsorption capacities and partition coefficient of different magnetite sorbents

Sorbents	pH	Temperature (°C)	Adsorbents dosage (g L^{-1})	Initial P concentration (mg L^{-1})	Final P concentration (mg L^{-1})	Maximum adsorption capacity (mg-P g^{-1})	Partition coefficient (mg g^{-1} μM^{-1})	Ref.
$Fe_3O_4/La(OH)_3$	7.0	25	0.1	10	4.73	52.7	0.35	15
$NaLa(CO_3)_2/Fe_3O_4$	6.8	25	0.1	50	42.215	77.85	0.06	16
Fe_3O_4/La-MOF	7.0	25	0.3	100	82.39	58.7	0.02	17
Fe_3O_4@MgAl-LDH@$La(OH)_3$	7.0	25	0.1	12	5.35	66.5	0.39	18
$Fe_3O_4/Al(OH)_3$	7.0	25	0.2	15	12.9	10.5	0.03	19
$Fe_3O_4/La(OH)_3$	7.0	25	0.2	15	11.14	19.3	0.05	19
$La(OH)_3/Fe_3O_4$	7.0	23	0.1	15	6.65	83.5	0.39	20
La_2-Al@Fe_3O_4	6.0	25	0.2	50	—	71.73	—	22
Fe_3O_4@LaAl-MOF	7.0	25	0.2	100	—	99.72	—	24
La Al co-loaded Fe_3O_4	—	—	0.1	50	40.57	94.3	0.07	23
Fe_3O_4/α-FeOOH/$Al(OH)_3$	7.0	25	0.1	15	5.51	94.9	0.53	This work

superior to most lanthanum- and aluminum-based magnetic composites. More significantly, the PC of MGA40 (0.53 mg g^{-1} μM^{-1}) is consistently higher than those of the evaluated adsorbents, excluding a few cases where the exact PC cannot be precisely calculated due to undisclosed solution volumes in the original literature. This notably high PC indicates that MGA40 exhibits a stronger intrinsic affinity for phosphate, driving a more effective transfer of phosphate from the aqueous phase to the solid surface. It should be noted that both the adsorption capacity and PC of MGA40 are substantially higher than those of the $Fe_3O_4/Al(OH)_3$ composite.[19] This enhancement is likely attributed to the higher $Al(OH)_3$ loading achieved in MGA40, whereas the $Fe_3O_4/Al(OH)_3$ composite contains only 5.95% Al.[19] Consequently, this suggests that utilizing goethite as the carrier facilitates a higher $Al(OH)_3$ loading, ultimately yielding superior phosphate adsorption performance.

3.3 Adsorption mechanism

To reveal the adsorption mechanism, FT-IR spectrum of MGA40 were recorded after phosphate adsorption, with the result depicted in Fig. 3a. Following adsorption, a new band emerges at 1031 cm^{-1}, which is assigned to the P–O asymmetric stretching vibration of PO_4^{3-},[68,69] thereby confirming the successful attachment of phosphate onto the MGA40 nanocomposite. Notably, the peaks at 977 and 1090 cm^{-1}, corresponding to the Al–O stretching and Al–OH symmetrical vibrations, disappear, indicating that the surface hydroxyl groups are consumed during the adsorption process, due to a ligand exchange interaction between the surface hydroxyl groups and phosphate species in solution.[70,71] Furthermore, the disappearance of the peaks at 1466, 1577, and 2850 cm^{-1}, along with the significant attenuation of the 2919 cm^{-1} band, indicates the involvement of surface Al-coordinated acetate complexes in the ligand exchange process.[50]

To further elucidate the surface complexation interactions, the chemical composition and electronic states of MGA40 before and after phosphate adsorption were analyzed using XPS. In the survey spectrum of the spent MGA40 (Fig. S5 and 6a), a distinct P 2p peak emerges at a binding energy of 134.2 eV, alongside the characteristic peaks of Fe, O, C, and Al observed in the pristine sample. This provides direct evidence for the successful immobilization of phosphate onto the composite. As illustrated in Fig. 3b and 6b, the binding energy of the Al 2p peak exhibits a noticeable positive shift from 75.05 eV before adsorption to 75.25 eV after adsorption. This shift toward higher binding energy indicates a reduction in the electron cloud density surrounding the Al atoms, which is characteristic of the formation of Al–O–P inner–sphere complexes *via* surface complexation.[72] The high-resolution O 1s spectra (Fig. 6c) can be deconvoluted into three distinct components at 530.6, 531.9, and 532.8 eV, corresponding to bulk oxygen (O_2^-), surface hydroxyl/phosphate groups (Al–OH/P–O), and oxygen atoms in the O–C=O group, respectively.[15,50,73,74] After adsorption, the relative area of the Al–OH/P–O peak increases significantly from 40.67% to 46.42%. This enhancement, coupled with the positive shift of Al 2p (Fig. 6b), strongly supports the formation of Al–O–P bonds *via* a ligand exchange mechanism, where incoming phosphate species replace surface hydroxyl groups.[15,19] Conversely, the proportion of the O–C=O component decreases from 30.08% to 23.03%, implying that the surface acetate anions are also consumed during this process. This is further corroborated by the high-resolution C 1s spectrum (Fig. 6d), which is resolved into C–C/C–H (284.7 eV), C–O (286.2 eV), and O–C=O (289.0 eV) peaks.[50,73] The proportional decline of the O–C=O peak from 11.39% to 9.32% in the C 1s spectrum suggests that the surface Al-acetate complexes actively participate in the ligand exchange process to facilitate phosphate binding. Together, FT-IR and XPS results show that MGA40 removes phosphate primarily by forming stable Al–O–P inner–sphere complexes. This process occurs *via* a dual ligand exchange mechanism involving surface hydroxyl and acetate species.

3.4 Influence of the coexistence of other anions

In the practical treatment of natural water bodies and industrial effluents, phosphate inevitably coexists with various

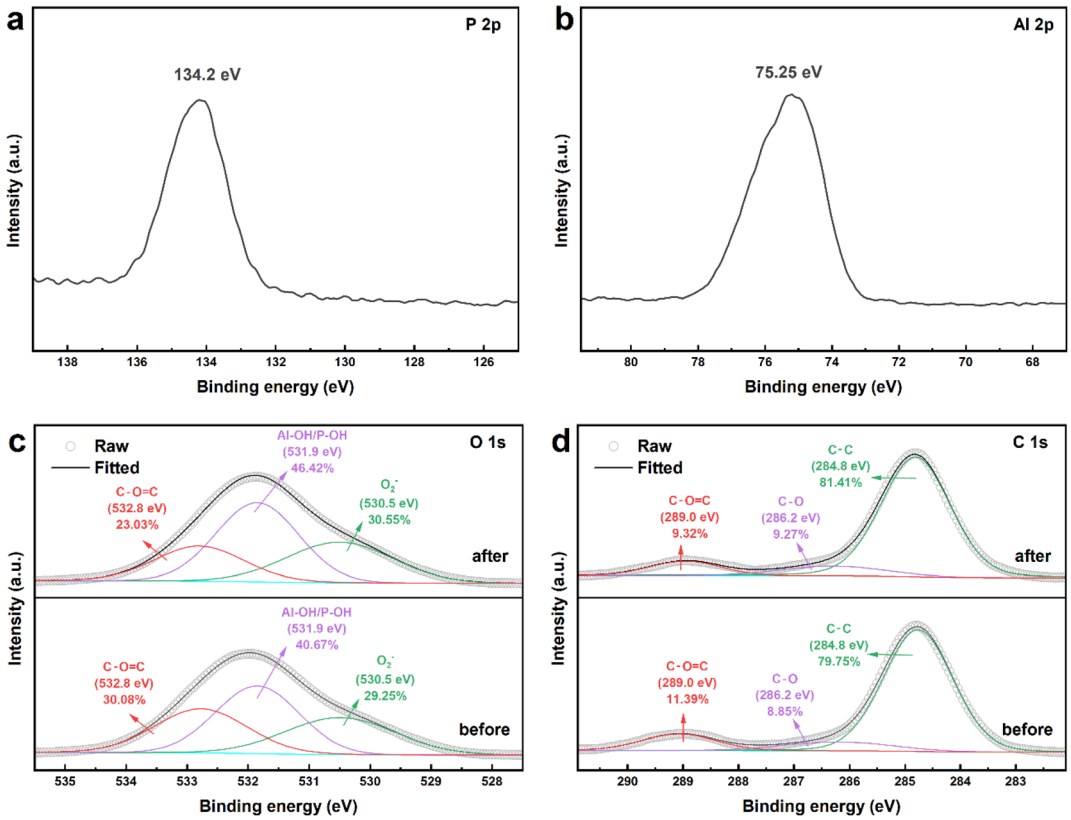

Fig. 6 High-resolution XPS spectra of P 2p (a) and Al 2p (b) of MGA40 nanocomposite after phosphate adsorption, and O 1 s (c) and C 1 s (d) of MGA40 nanocomposite before and after phosphate adsorption.

background anions.[75,76] Therefore, evaluating the adsorption selectivity of MGA40 for phosphate is of critical importance. Beyond commonly investigated inorganic anions such as Cl^-, NO_3^-, SO_4^{2-} and HCO_3^-, high concentrations of organic acids may compete with phosphate for adsorption sites, with acetic acid being one of the most abundant components in actual polluted water.[75] To simulate realistic conditions, the initial phosphate concentration was fixed at 10 mg L^{-1}, while the coexisting ions were introduced at 10 and 100 mg L^{-1}, which represent the typical concentration range of anions in wastewater.[76] As for acetate, Xiao *et al.* reported that the acetic acid concentration in lake sediment pore waters averages around 3.8 mg L^{-1}, reaching a maximum of 9.8 mg L^{-1}.[77] Furthermore, its concentration in industrial wastewater is generally between 30.0 and 83.5 mg L^{-1}.[75] Accordingly, the tested concentrations of 10 and 100 mg L^{-1} also effectively cover the typical abundance of acetic acid in actual polluted water systems. As illustrated in Fig. S6, these competitive anions, even at a high concentration of 100 mg L^{-1}, exert negligible interference on phosphate adsorption, demonstrating the exceptional selectivity of MGA40 for phosphate. More importantly, the presence of aqueous acetate ions does not inhibit phosphate adsorption. Considering that surface-bound acetate actively participates in the ligand exchange mechanism, this finding further confirms the rationale of employing sodium acetate as the weak base source during the synthesis of MGA40, proving that it induces no negative impacts on subsequent applications.

3.5 Effects of pH on phosphate adsorption and environmental friendliness assessment

The pH of aqueous environments can vary considerably and is often subject to dynamic fluctuations. In eutrophic lakes, intense photosynthetic activity by algae consumes dissolved carbon dioxide, frequently elevating the water pH to a range of 7.0–9.0,[78,79] and occasionally up to 10.0–10.5 under extreme bloom conditions.[80,81] To simulate these environmentally relevant conditions, the phosphate adsorption capacity of MGA40 was evaluated across an initial pH range of 4.0 to 11.0 (Fig. 7a). The results reveal a slight increase in adsorption capacity from pH 4 to 5, followed by a gradual decline between pH 5 and 10, and a sharp decrease at pH 11. This pH-dependent trend can be attributed to the surface charge characteristics of MGA40. As shown in Fig. S7, the point of zero charge (pH_{pzc}) of MGA40 is 8.33, indicating that the material surface becomes negatively charged at pH values above 8.33. Furthermore, $Al(OH)_3$, the primary active component for phosphate binding, undergoes alkaline dissolution at pH >8 to form soluble $Al(OH)_4^-$. This transformation causes a loss of active adsorption sites and exacerbates electrostatic repulsion between the negatively charged surface and phosphate anions, hindering adsorption.[82]

Notably, the reduction in adsorption capacity of MGA40 is relatively modest between pH 6 and 10, which may be explained by a surface-induced pH-lowering effect. For initial pH values of 9 and 10, the equilibrium pH falls below 8.0 (Fig. 7b), allowing MGA40 to maintain its structural stability and favorable surface

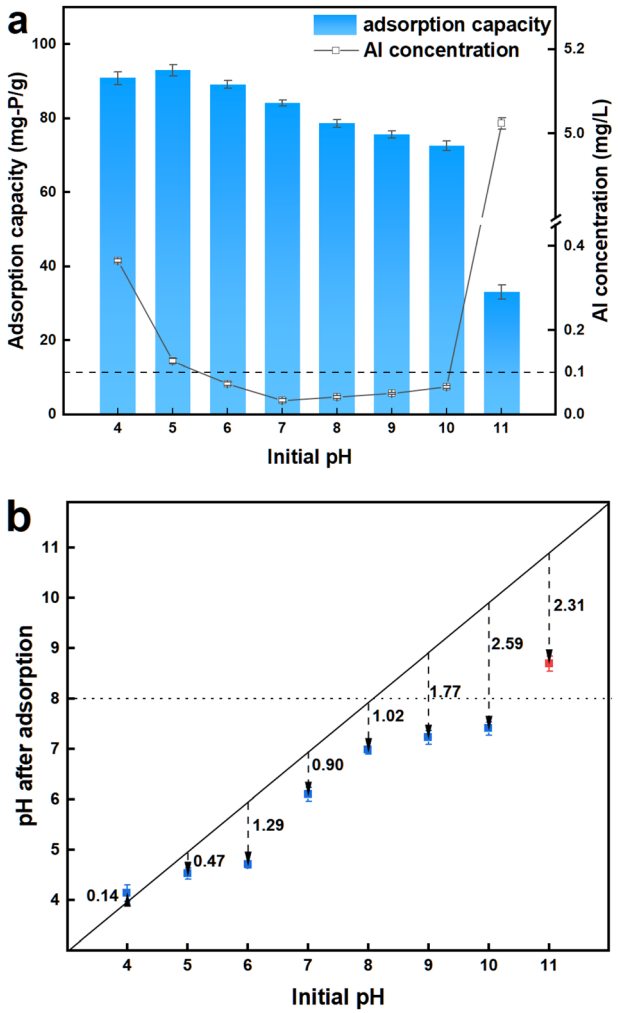

Fig. 7 Effect of initial solution pH on the phosphate adsorption capacity of MGA40, dissolved aluminum concentration in solutions (a), and solution pH after adsorption (b).

charge while mitigating competition from hydroxyl ions. In contrast, at an initial pH of 11, the final pH remains above 8.0, resulting in severe adsorption capacity loss. Similar observations have been reported for aluminum-modified zeolite (AMZ), where the material lowered the solution pH by 1.8 and 2.4 units at start pH 9 and 10, and decreased sediment pH by 0.3–0.5 units to sustain phosphate uptake under alkaline conditions.[83] Consequently, this pH-lowering effect suggests that MGA40 similarly holds potential value for practical applications.

To evaluate potential ecotoxicological risks, dissolved aluminum leaching was monitored during the sorption process across the pH 4.0–11.0 range. As shown in Fig. 7a, the dissolved aluminum concentration gradually decreases from 0.36 to 0.03 mg L^{-1} as the pH increases from 4.0 to 7.0, with a marginal increase to 0.06 mg L^{-1} at pH 10.0. However, a significant release of 5.02 mg L^{-1} occurs at pH 11.0, likely due to the alkaline dissolution of aluminum hydroxide. Within the environmentally relevant pH range of 6.0 to 10.0, these laboratory-derived aluminum concentrations remain uniformly low, consistently falling below 0.10 mg L^{-1}, a level strictly below the toxicity thresholds known to adversely impact phytoplankton and invertebrates, and which complies with the recommended upper limit for dissolved Al in hard water lakes.[84,85] Reitzel *et al.* demonstrated that while elevated pH can induce aluminum release in lakes treated with traditional aluminum salts, it generally does not trigger significant toxicological events.[86] Given that aluminum hydroxide is the primary active species responsible for phosphorus adsorption formed after adding aluminum salts to water, the environmental risk of secondary aluminum pollution from MGA40, which holds the same active component, is likely minimal, further confirming its ecological safety.

3.6 Adsorption–desorption cycles

Considering the rationale for utilizing aluminum-based materials in phosphate recovery and the pH-dependent adsorption behavior of MGA40, a 0.1 mM NaOH solution was selected as the eluent for five adsorption–desorption cycles (Fig. 8). Throughout the cycles, the desorption efficiency was maintained at approximately 72%, comparable to that of other magnetic adsorbents requiring 1.0 M NaOH,[18,19] although the gradual decline in adsorption capacity can be attributed to the alkaline dissolution of aluminum hydroxide at this pH (>8.0). Nevertheless, MGA40 retained a competitive adsorption capacity of 52.3 mg-P g^{-1} after five cycles, which is still higher than those of many fresh adsorbents listed in Table 2. The stability of the adsorbent is significant for its practical applications.[87] Therefore, the XRD pattern of regenerated MGA40 after five adsorption–desorption cycles was obtained and presented in Fig. S8. The characteristic peaks of goethite and magnetite were retained in the post-cycling sample, indicating that the main crystalline phases of MGA40 remained stable after repeated use. No new crystalline peaks were observed after cycling, suggesting that no newly formed crystalline aluminum hydroxide phase was detected in the regenerated adsorbent. These results further demonstrate the good stability and reusability of MGA40 as a magnetic adsorbent for phosphate

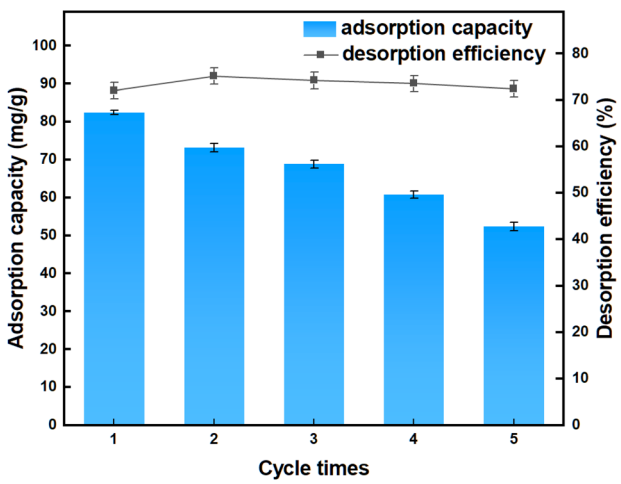

Fig. 8 Phosphate adsorption capacity and desorption efficiency of MGA40 in five adsorption–desorption cycles.

adsorption. In addition, achieving desorption without extreme pH conditions suggests potential value for slow-release fertilizer production,[60] though this warrants further investigation beyond the scope of the current study.

4. Conclusion

In summary, a novel magnetic nanocomposite (Fe_3O_4/α-FeOOH/$Al(OH)_3$, MGA) was successfully fabricated *via* a facile one-pot method for efficient phosphate recovery. The optimal MGA delivered a maximum phosphate adsorption capacity of 94.9 mg-P g^{-1} and a high partition coefficient of 0.53 mg g^{-1} μM^{-1} at pH 7.0. This exceptional adsorption performance was maintained across a broad environmentally relevant pH range (6.0–10.0), exhibiting remarkable selectivity even in the presence of ubiquitous competing anions. Mechanistic investigations confirmed that phosphate capture is primarily driven by ligand exchange, resulting in the formation of robust inner-sphere complexes with the surface-loaded amorphous aluminum hydroxide. Crucially, dissolved aluminum leaching during the adsorption process remained strictly below ecotoxicity thresholds across the pH range 6.0–10.0, confirming the ecological safety of MGA for practical applications. Moreover, spent MGA can be readily recovered *via* magnetic separation and efficiently regenerated using a dilute NaOH solution, sustaining a competitive adsorption capacity over five consecutive cycles. Overall, this study presents a cost-effective and environmentally safe adsorbent for phosphorus removal, highlighting its potential for sustainable resource recycling.

Author contributions

Yu-Han Wang: conceptualization, methodology, data curation, writing – original draft preparation. Wei Yin: data curation, software. Wen-Ping Liu: visualization, investigation. Qi-Zhi Yao: formal analysis, validation. Sheng-Quan Fu: methodology, resources. Gen-Tao Zhou: supervision, writing – reviewing and editing, funding acquisition.

Conflicts of interest

There are no conflicts to declare.

Data availability

The data that support the findings of this study are available from the corresponding author on reasonable request.

Supplementary information (SI) is available. See DOI: https://doi.org/10.1039/d6ra01891b.

Acknowledgements

This work was partially supported by the National Natural Science Foundation of China (Nos. 42430201), the Anhui Provincial Natural Science Foundation (No. 2408085QD120), and the Fundamental Research Funds for the Central Universities (No. WK2080000194).

References

1 J. Elser and E. Bennett, *Nature*, 2011, **478**, 29–31.
2 Y. Lan, S. Gai, K. Cheng and F. Yang, *Environ. Sci. Water Res. Technol.*, 2022, **8**, 1173–1187.
3 Y. Luo, H. Li, Y.-R. Huang, T.-L. Zhao, Q.-Z. Yao, S.-Q. Fu and G.-T. Zhou, *Chem. Eng. J.*, 2018, **351**, 195–202.
4 C. Zhang, A. Guisasola and J. A. Baeza, *Water Res.*, 2022, **212**, 118102.
5 M. Geng, W. Zhang, T. Hu, R. Wang, X. Cheng and J. Wang, *Water Res.*, 2022, **210**, 118003.
6 J. Zhou, P. R. Leavitt, Y. Zhang and B. Qin, *Water Res.*, 2022, **221**, 118728.
7 L. Kang, S. Haasler, M. Mucci, L. Korving, A. I. Dugulan, T. Prot, G. Waajen and M. Lürling, *Water Res.*, 2023, **244**, 120391.
8 P. Zhang, M. He, S. Huo, F. Li and K. Li, *Chem. Eng. J.*, 2022, **446**, 137081.
9 C. V. Flores, J. L. Obeso, L. Herrera-Zuñiga, R. A. Peralta, J. I. Campero-Domínguez, L. Morales-Ruiz, N. S. Portillo-Vélez and J. C. Valdivia-Corona, *RSC Sustain.*, 2026, **4**, 61–78.
10 A. S. Eltaweil, E. M. A. El-Monaem, H. M. Elshishini, H. G. El-Aqapa, M. Hosny, A. M. Abdelfatah, M. S. Ahmed, E. N. Hammad, G. M. El-Subruiti, M. Fawzy and A. M. Omer, *RSC Adv.*, 2022, **12**, 8228–8248.
11 A. Funes, J. de Vicente, L. Cruz-Pizarro, I. Álvarez-Manzaneda and I. de Vicente, *Water Res.*, 2016, **89**, 366–374.
12 J. Lin, Y. Li, Y. Zhan and X. Wu, *Water Res.*, 2023, **235**, 119899.
13 M. H. P. Araújo, L. M. F. Moreira, J. D. Ardisson, R. M. Lago and J. C. Tristão, *RSC Sustain.*, 2026, **4**, 1393–1408.
14 V. Gök, Ö. Topel and S. Aksu, *New J. Chem.*, 2022, **46**, 14466–14478.
15 L. Fang, R. Liu, J. Li, C. Xu, L.-Z. Huang and D. Wang, *Water Res.*, 2018, **130**, 243–254.
16 H. Hao, Y. Wang and B. Shi, *Water Res.*, 2019, **155**, 1–11.
17 Q. He, H. Zhao, Z. Teng, Y. Wang, W. Sun, Y. Guo, X. Ji, W. Hu, S. Shiung Lam and M. Li, *Sep. Purif. Technol.*, 2023, **314**, 123529.
18 Z. Lin and J. Chen, *Chemosphere*, 2021, **264**, 128551.
19 Q. Song, S. Huang, L. Xu, N. Wang, Z. Hu, X. Luo and Z. Zheng, *Sci. Total Environ.*, 2020, **723**, 137838.
20 B. Wu, L. Fang, J. D. Fortner, X. Guan and I. M. C. Lo, *Water Res.*, 2017, **126**, 179–188.
21 X. Lu, Z. Zhong, R. Yan, F. Zan, W. Lou, J. Liu, X. Wu and B. Zhang, *J. Clean. Prod.*, 2022, **373**, 133746.
22 G. Zhang, H. He, S. Liu, Z. Du, L. Lv, L. Sun, J. Zhang and J. Liang, *J. Water Process Eng.*, 2024, **68**, 106344.
23 Z. Long, H. He, H. Song, J. Liang and G. Zhang, *Chem. Eng. J.*, 2025, **522**, 167989.
24 Q. Zhang, B. Lei, R. Xiong, B. Wu, Q. Li, Z. Zhang, C. Yv, X. Yang and S. Li, *Appl. Surf. Sci.*, 2026, **722**, 165578.
25 G. W. Kajjumba and E. J. Marti, *Chemosphere*, 2022, **309**, 136462.
26 Y. Zhi, C. Zhang, R. Hjorth, A. Baun, O. W. Duckworth, D. F. Call, D. R. U. Knappe, J. L. Jones and K. Grieger, *Environ. Int.*, 2020, **145**, 106115.

27 O. Agstam-Norlin, E. E. Lannergård, E. Rydin, M. N. Futter and B. J. Huser, *Water Res.*, 2021, **200**, 117267.
28 I. de Vicente, P. Huang, F. Ø. Andersen and H. S. Jensen, *Environ. Sci. Technol.*, 2008, **42**, 6650–6655.
29 S. Gypser, F. Hirsch, A. M. Schleicher and D. Freese, *J. Environ. Sci.*, 2018, **70**, 175–189.
30 B. J. Huser, S. Egemose, H. Harper, M. Hupfer, H. Jensen, K. M. Pilgrim, K. Reitzel, E. Rydin and M. Futter, *Water Res.*, 2016, **97**, 122–132.
31 T. Dadi, M. Schultze, X. Kong, M. Seewald, K. Rinke and K. Friese, *Water Res.*, 2023, **235**, 119824.
32 Y.-Y. Chen, S.-H. Yu, Q.-Z. Yao, S.-Q. Fu and G.-T. Zhou, *J. Colloid Interface Sci.*, 2018, **510**, 280–291.
33 X. Jin, J. Guo, M. F. Hossain, J. Lu, Q. Lu, Y. Zhou and Y. Zhou, *Resour. Conserv. Recycl.*, 2024, **204**, 107464.
34 H. Jin, X. Tian, Y. Nie, Z. Zhou, C. Yang, Y. Li and L. Lu, *Environ. Sci. Technol.*, 2017, **51**, 12699–12706.
35 H. Feng, S. Ma, Z. Chen, Y. Li, M. Wang and Y. Ding, *Environ. Sci. Nano*, 2024, **11**, 2655–2667.
36 Y. Liang, D. Yu, J. Jin, J. Xiong, J. Hou, M. Wang and W. Tan, *Sci. Total Environ.*, 2021, **790**, 148202.
37 Y. Shao, G. Hu, Z. Liu, X. Xu, M. Zhang, C. Ding and Y. Li, *Materials*, 2022, **15**, 1465.
38 L.-C. Hsu, Y.-M. Tzou, M.-S. Ho, C. Sivakumar, Y.-L. Cho, W.-H. Li, P.-N. Chiang, H. Y. Teah and Y.-T. Liu, *Environ. Sci. Nano*, 2020, **7**, 3497–3508.
39 E. R. Encina, M. Distaso, R. N. Klupp Taylor and W. Peukert, *Cryst. Growth Des.*, 2015, **15**, 194–203.
40 F. Gilbert, P. Refait, F. Lévêque, C. Remazeilles and E. Conforto, *J. Phys. Chem. Solids*, 2008, **69**, 2124–2130.
41 Q. Hao, S. Liu, X. Yin, Y. Wang, Q. Li and T. Wang, *Solid State Sci.*, 2010, **12**, 2125–2129.
42 G. Wang, M. E. Bowden, S. A. Saslow, B. J. Riley, D.-S. Kim, W. C. Eaton and A. A. Kruger, *J. Nucl. Mater.*, 2021, **552**, 152964.
43 J. Murphy and J. P. Riley, *Anal. Chim. Acta*, 1962, **27**, 31–36.
44 L. Mei, L. Liao, Z. Wang and C. Xu, *Adv. Mater. Sci. Eng.*, 2015, **2015**, 250836.
45 N. T. Vinh, L. A. Tuan, L. K. Vinh and N. Van Quy, *Mater. Sci. Semicond. Process.*, 2020, **118**, 105211.
46 A. E. Lavat, M. C. Grasselli and E. G. Lovecchio, *Ceram. Int.*, 2010, **36**, 15–21.
47 C. Zhang, H. Li, X. Guo, S. Li, H. Zhang, X. Pan and M. Hua, *Powder Technol.*, 2021, **393**, 280–290.
48 C. Han, H. Pu, H. Li, L. Deng, S. Huang, S. He and Y. Luo, *J. Hazard. Mater.*, 2013, **254–255**, 301–309.
49 P. Persson, M. Karlsson and L.-O. Öhman, *Geochim. Cosmochim. Acta*, 1998, **62**, 3657–3668.
50 Y.-X. Zhang and Y. Jia, *J. Colloid Interface Sci.*, 2016, **483**, 295–306.
51 Z. Wu, C. Zhao, W. Zeng, X. Wang, C. Liu, Z. Yu, J. Zhang and Z. Qiu, *Chem. Eng. J.*, 2022, **448**, 137464.
52 S. C. Peterangelo, R. T. Hart and A. E. Clark, *J. Phys. Chem. B*, 2007, **111**, 7073–7077.
53 L. Zhu, S. Pu, F. Lu, K. Liu, T. Zhu, J. Li and J. Li, *Mater. Chem. Phys.*, 2012, **135**, 979–984.
54 J. Chen, R. Yang, Z. Zhang and D. Wu, *J. Hazard. Mater.*, 2022, **421**, 126817.
55 S. Thomas and P. M. Sherwood, *Anal. Chem.*, 1992, **64**, 2488–2495.
56 Y. Zhang, J. Chen, H. Zhang, S. Gong, Y. Xiao and L. Huang, *J. Clean. Prod.*, 2024, **435**, 140537.
57 Y. Yao, R. Pan, H. Cheng, Y. Gong, L. Chen, X. Zhang, M. Xue and X. Tian, *Colloids Surf. A Physicochem. Eng. Asp.*, 2025, **727**, 138378.
58 R. Barik, B. K. Jena and M. Mohapatra, *RSC Adv.*, 2017, **7**, 49083–49090.
59 W. Zhang, R. Zhao, B. Bao, S. Liu, C. Hu, W. Ding and H. Zheng, *Sep. Purif. Technol.*, 2023, **325**, 124741.
60 I. D. Borges, C. M. Rocha, F. Maia, C. M. Silva and M. J. Quina, *RSC Adv.*, 2025, **15**, 45427–45437.
61 W. Plazinski, W. Rudzinski and A. Plazinska, *Adv. Colloid Interface Sci.*, 2009, **152**, 2–13.
62 Z. Tan, X. Fan, Q. Fan, S. Lu, T. Yu, L. Ma, Y. Luo, J. Li, H. Li and Y. Hu, *Chem. Eng. Sci.*, 2025, **302**, 120908.
63 X. Zhang, H. Yao, X. Lei, Q. Lian, A. Roy, D. Doucet, H. Yan, M. E. Zappi and D. D. Gang, *Environ. Res.*, 2021, **199**, 111223.
64 B. Liu, S. Gai, Y. Lan, K. Cheng and F. Yang, *Environ. Res.*, 2022, **212**, 113353.
65 M. A. Al-Ghouti and D. A. Da'ana, *J. Hazard. Mater.*, 2020, **393**, 122383.
66 J. J. Hurst, J. S. Wallace and D. S. Aga, *Chemosphere*, 2018, **197**, 271–279.
67 K. Vikrant and K.-H. Kim, *Chem. Eng. J.*, 2019, **358**, 264–282.
68 X.-H. Guan, Q. Liu, G.-H. Chen and C. Shang, *J. Colloid Interface Sci.*, 2005, **289**, 319–327.
69 P.-A. Mouthuy, A. Crossley and H. Ye, *Mater. Lett.*, 2013, **106**, 145–150.
70 L. Feng, Q. Zhang, F. Ji, L. Jiang, C. Liu, Q. Shen and Q. Liu, *Chem. Eng. J.*, 2022, **430**, 132754.
71 S. Li, J. Shao, B. Ma, B. Wu and C. Hu, *Chem. Eng. J.*, 2023, **464**, 142589.
72 Q.-X. Song, Y.-X. Xu, N. Fang, J. Liu and H.-L. Zhu, *J. Environ. Chem. Eng.*, 2023, **11**, 111418.
73 V. Datsyuk, M. Kalyva, K. Papagelis, J. Parthenios, D. Tasis, A. Siokou, I. Kallitsis and C. Galiotis, *Carbon*, 2008, **46**, 833–840.
74 S. Rahman, C. M. Navarathna, N. Krishna Das, J. Alchouron, P. Reneau, S. Stokes, R. V. K. G. Thirumalai, F. Perez, E. Barbary Hassan, D. Mohan, C. U. Pittman and T. Mlsna, *J. Colloid Interface Sci.*, 2021, **597**, 182–195.
75 J. Cui, J. Yang, M. Weber, J. Yan, R. Li, T. Chan, Y. Jiang, T. Xiao, X. Li and X. Li, *Water Res.*, 2023, **234**, 119804.
76 C. Warwick, A. Guerreiro and A. Soares, *Biosens. Bioelectron.*, 2013, **41**, 1–11.
77 M. Xiao, F. C. Wu, H. Q. Liao, W. Li, X. Q. Lee and R. S. Huang, *J. Hydrol.*, 2009, **365**, 37–45.
78 X. Cao, Y. Wang, J. He, X. Luo and Z. Zheng, *Environ. Pollut.*, 2016, **219**, 580–587.
79 R. G. Wetzel, *Limnology: Lake and River Ecosystems*, gulf professional publishing, 2001.
80 A. I. López-Archilla, D. Moreira, P. López-García and C. Guerrero, *Extremophiles*, 2004, **8**, 109–115.

81 M. Mucci, V. Maliaka, N. P. Noyma, M. M. Marinho and M. Lürling, *Sci. Total Environ.*, 2018, **619–620**, 1431–1440.
82 D. A. Georgantas and H. P. Grigoropoulou, *J. Colloid Interface Sci.*, 2007, **315**, 70–79.
83 L. Kang, M. Mucci and M. Lürling, *Sci. Total Environ.*, 2022, **812**, 151489.
84 R. A. Freeman and W. H. Everhart, *Trans. Am. Fish. Soc.*, 1971, **100**, 644–658.
85 R. W. Gensemer and R. C. Playle, *Crit. Rev. Environ. Sci. Technol.*, 1999, **29**, 315–450.
86 K. Reitzel, H. S. Jensen and S. Egemose, *Water Res.*, 2013, **47**, 1409–1420.
87 V. Ganesan, C. Louis and S. P. Damodaran, *J. Environ. Chem. Eng.*, 2018, **6**, 2176–2190.